nature aging

Supplementary information

https://doi.org/10.1038/s43587-026-01219-7

RamanOmics decodes the spatial vibrational–molecular architecture of senescence in aging and repair

In the format provided by the authors and unedited

Supplementary Note 1

Increased cell-cell interactions and ECM remodeling in aging

Next, we examined how aging alters intercellular communication. We first assessed interactions of lung endothelial cells and T cells, and skin IFE cells and fibroblasts with other cell types, as these populations showed prominent age-related transcriptomic alterations (**Fig. 1d**). In old lung, endothelial cell subtypes demonstrated a global reduction in cell-cell interactions, including diminished endothelial self-communication (**Supplementary Fig. 4a**). In contrast, we observed increased interactions between T cells and monocytes, dendritic cells, and AT2-2 cells (**Supplementary Fig. 4a**). Similarly, in old skin, FIB and IFE cells showed decreased interactions with most other cell types yet exhibited enhanced communication between IFE and sebocytes (**Supplementary Fig. 4b**).

To further explore how these changes translate into signaling dynamics, we analyzed age-associated pathway activity across lung and skin tissues. In the old lung, TGF-β signaling was prominently upregulated in Endo5, SMC1/2, and FIB populations, while AT1-1 and AT2-1 cells displayed elevated collagen signaling relative to young samples (**Supplementary Fig. 4c**). These pathways are classically associated with fibrosis, vascular remodeling, and senescence, suggesting a shift toward a pro-fibrotic and inflammatory microenvironment with age[1–3]. In the old skin, Notch signaling was enhanced in FIB3, IFE3 and IFK populations, whereas BMP signaling increased in OBC, FIB3 and IFE3 cells (**Supplementary Fig. 4d**), indicating a transition toward differentiation, matrix remodeling, and altered epithelial homeostasis[4–7].

To examine how these age-related signaling changes intersect with cellular senescence, we next focused on cell-cell interactions involving senescent cells. In the lung, *p21*$^{+}$ AT2-2 and T cells exhibited increased interactions with both senescent and non-senescent cells compared to their younger counterparts (**Supplementary Fig. 5a**), suggesting that senescent cells actively engage in shaping their local microenvironment. In contrast, in old skin, *p21*$^{+}$ IFE4 and Langerhans cells predominantly increased interactions with non-senescent neighbors (**Supplementary Fig. 5b**), possibly reflecting their roles in epithelial surveillance and immune crosstalk.

We further analyzed signaling pathway activation in senescent cells to understand the functional implications of these interactions. In old lung, senescent AT2-2 cells, T cells, macrophages, and monocytes showed heightened TGF-β signaling, while senescent AT2-2 cells, T cells, monocytes, and FIB2 displayed increased collagen signaling compared to young tissues (**Supplementary Fig. 5c**). These pathways, known drivers of ECM remodeling, fibrosis, and senescence[1–3], point to a microenvironment that sustains and amplifies senescent cell states. Similarly, in the old skin, senescent IFE and IFK cells exhibited elevated Notch and BMP signaling (**Supplementary Fig. 5d**), consistent with enhanced epithelial differentiation and remodeling during cutaneous aging[4,7].

Supplementary Note 2

Increased cell size in senescence

To assess how aging and senescence affect cellular morphology, given that size changes are key indicators of altered cellular function, metabolic state, and structural adaptations during aging across different tissues[8], we analyzed cell sizes using single-cell segmentation from registered STARmap data. Overall, cells in old tissues were significant smaller than those in young tissues (lung: 8.84±3.86 vs 9.84±3.90, p-value (p)= 3.55E-64; skin: 11.93±6.51 vs 12.84±6.24, p= 6.58E-23) (**Supplementary Fig. 6a**); however, no significant differences in cell size were observed in Endo and IFE cells across age groups (**Supplementary Fig. 6d**). In contrast, *p21*$^{+}$ senescent cells were consistently larger than their non-senescent counterparts in old skin tissues (**Supplementary Fig. 6e**). In the lung, only *p21*$^{+}$ senescent mesenchymal cells (MES) showed a significant increase in size compared to non-senescent cells (13.6000±4.1593 vs. 9.2718±3.8256, p= 2.24E-02) (**Supplementary Fig. 6b**). In the skin, both global *p21*$^{+}$ senescent cells (13.8242±8.2484 vs. 11.8921±6.4650, p= 2.70E-02) and *p21*$^{+}$ senescent IFE cells (16.0952±9.9236 vs. 12.8356±6.9811, p= 3.04E-02), were significantly larger than their non-senescent counterparts in old tissues, and a similar trend was observed in young skin, where global *p21*$^{+}$ senescent cells (16.8182±8.4427 vs. 12.7565±6.1567, p= 1.76E-09) were markedly larger than non-senescent cells (**Supplementary Fig. 6e**). Interestingly, comparisons between senescent cells in young and old tissues revealed a size reduction in old skin tissues (13.8242±8.2484 vs. 16.8182±8.4427, p= 2.22E-03) (**Supplementary Fig. 6c**). These findings suggest that, while senescent cells generally exhibit increased size in skin tissues, aging may drive a reduction in cell size, potentially indicating age-related morphological and functional changes. This size variation could reflect differential senescence dynamics across tissues and age groups, highlighting tissue-specific adaptations during aging.

Methods

Cell-cell communication analysis

For inferring the cell-cell communications among cell types from senescent and non-senescent cells, CellChat (v2.1.2)[9] was used. Cell groups are defined using a combination of senescence status and cell type. Communication probability was computed using population.size= TRUE. Only cell-cell communications found in more than 10 cells in each group were considered for both senescent and non-senescent cells.

Cell size analysis

For Raman image analysis, cell size was quantified as the number of Raman pixels within each cell boundary, while cell intensity was calculated as the mean peak intensity across all pixels within each cell. Statistical differences between groups were assessed using the Mann–Whitney U test, and only differences with an FDR-adjusted $P \leq 0.05$ were considered statistically significant.

References

1. Frangogiannis, N. Transforming growth factor-β in tissue fibrosis. *J. Exp. Med.* **217**, e20190103 (2020).
2. Tominaga, K. & Suzuki, H. I. TGF-β signaling in cellular senescence and aging-related pathology. *Int. J. Mol. Sci.* **20**, 5002 (2019).
3. Leitinger, B. Discoidin domain receptor functions in physiological and pathological conditions. *Int. Rev. Cell Mol. Biol.* **310**, 39–87 (2014).
4. Zieba, J. T., Chen, Y.-T., Lee, B. H. & Bae, Y. Notch signaling in skeletal development, homeostasis and pathogenesis. *Biomolecules* **10**, 332 (2020).
5. Parambath, S., Selvraj, N. R., Venugopal, P. & Aradhya, R. Notch signaling: An emerging paradigm in the pathogenesis of reproductive disorders and diverse pathological conditions. *Int. J. Mol. Sci.* **25**, 5423 (2024).
6. Fessing, M. Y. *et al.* BMP signaling induces cell-type-specific changes in gene expression programs of human keratinocytes and fibroblasts. *J. Invest. Dermatol.* **130**, 398–404 (2010).
7. Botchkarev, V. A. & Sharov, A. A. BMP signaling in the control of skin development and hair follicle growth. *Differentiation* **72**, 512–526 (2004).
8. Lengefeld, J. *et al.* Cell size is a determinant of stem cell potential during aging. *Sci. Adv.* **7**, eabk0271 (2021).
9. Jin, S., Plikus, M. V. & Nie, Q. CellChat for systematic analysis of cell-cell communication from single-cell transcriptomics. *Nat. Protoc.* **20**, 180–219 (2025).

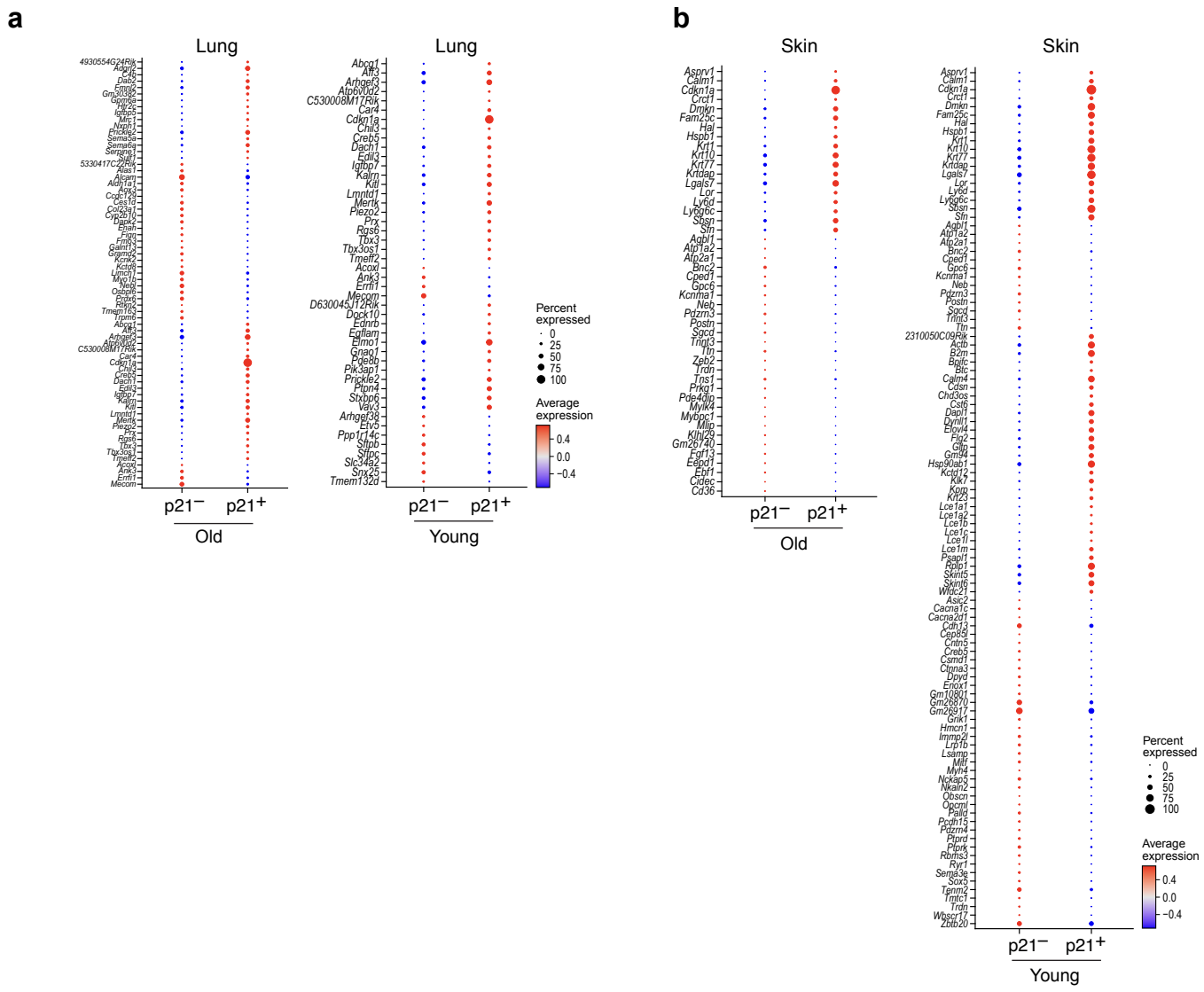

Supplementary Fig. 1. Further characterization of single-nucleus transcriptomic data for senescence analysis.

a-b, Dot plots showing DEGs enriched in p21+ senescent cells from old or young mouse lung (a) and skin (b). Average expression scores were calculated using log-normalized and scaled data (FDR<0.05). The numerical details are reported in Supplementary Table 2.

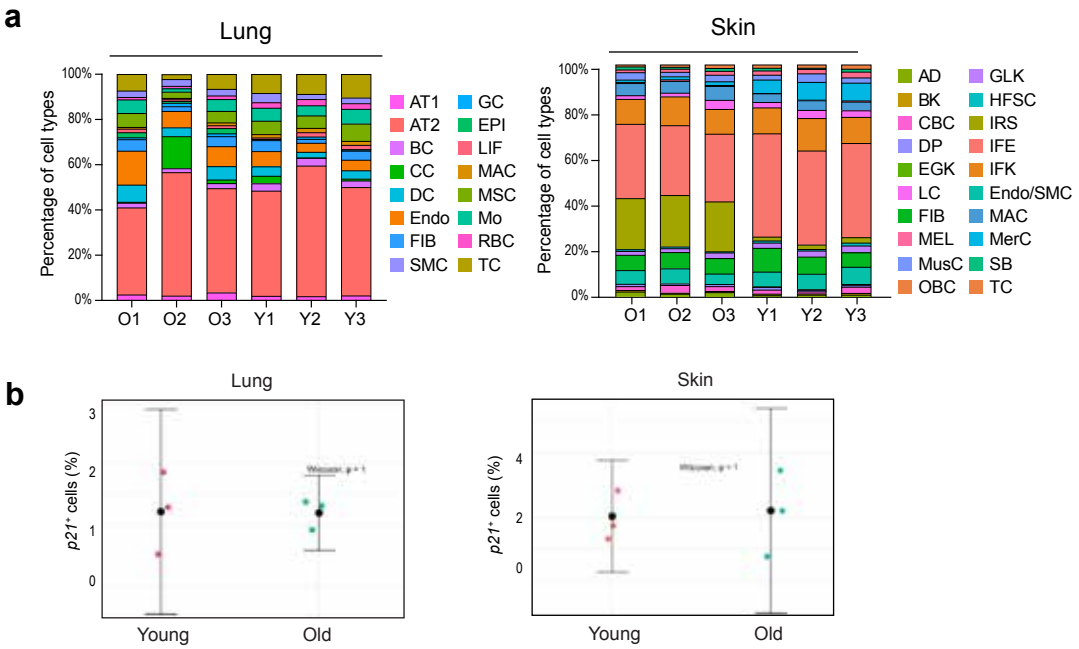

Supplementary Fig. 2. Cell-type composition and *p21*$^{+}$ cell proportion in young and old mouse tissues. **a**, Bar plots showing the relative abundance of each cell type in the Raman-STARmap co-registered dataset in mouse lung (left) and mouse skin (right). Cell types are colored according to STARmap-ISS cell-type annotation. **b**, Dot plots showing the proportion of *p21*$^{+}$ cells per biological replicate (n = 3 per condition, colored dots) with group mean and standard deviation (black dot and error bars) in young and old mouse lung (left) and skin (right), quantified from the Raman-imaged area. p-values indicate two-sided Wilcoxon rank-sum test comparing young versus old groups.

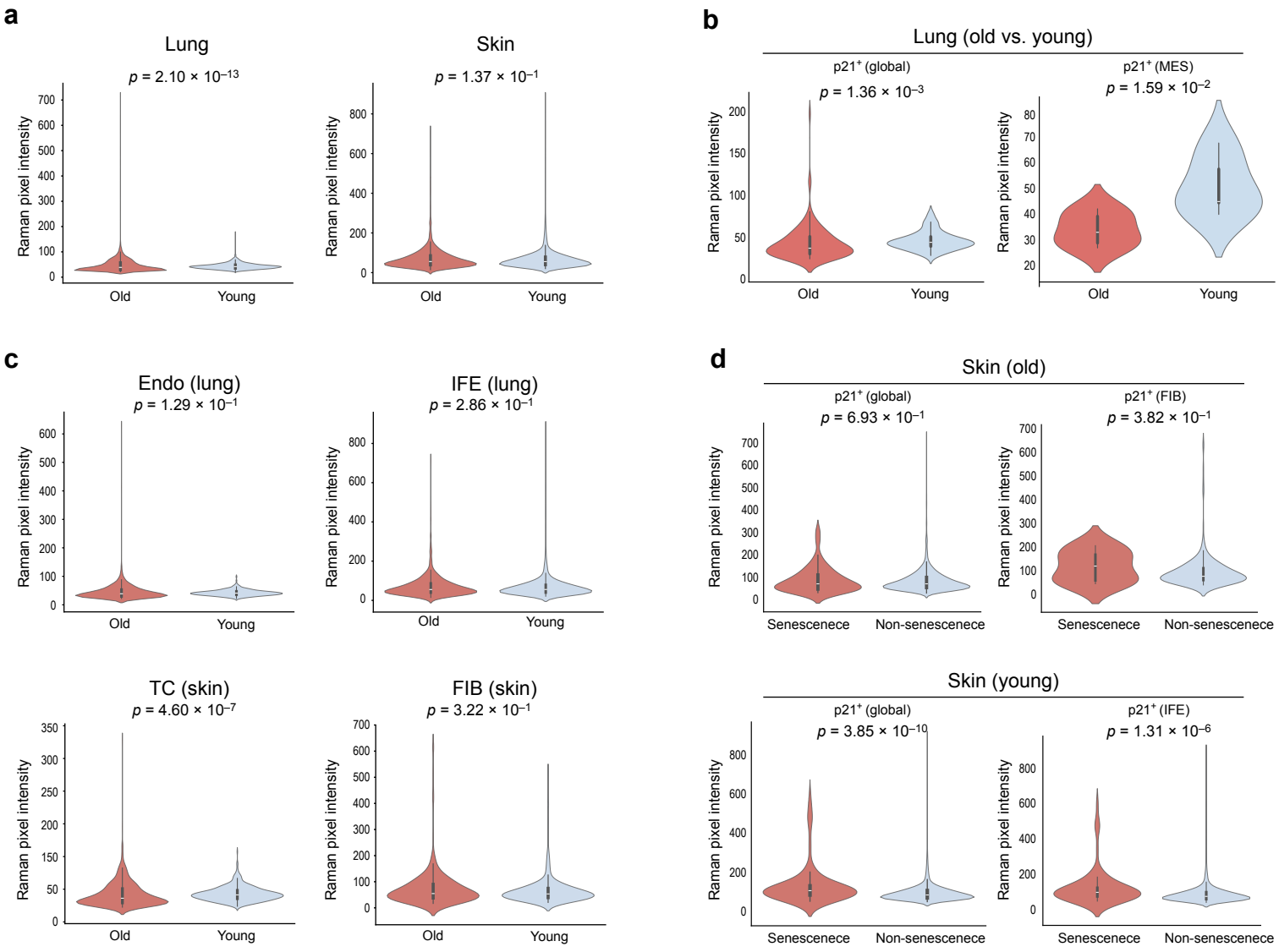

Supplementary Fig.3. Comparative analysis of average Raman intensity differences across tissues, ages and senescence status.

a, Violin plots showing the distribution of mean Raman spectral intensity per cell in young and old mouse lung and skin at tissue level. **b**, Violin plots showing the distribution of mean Raman spectral intensity per cell in tissue-level *p21*$^{+}$ cells and *p21*$^{+}$ mesenchymal cells from old and young mouse lung. **c**, Violin plots showing the distribution of mean Raman spectral intensity per cell across cell types in young and old mouse lung and skin. **d**, Violin plots showing the distribution of mean Raman spectral intensity per cell in *p21*$^{+}$ senescent cells and *p21*$^{-}$ non-senescent cells at tissue and cell-type levels in old and young mouse skin. p-value is calculated by the Mann-Whitney U test. For **a-d**, each cell represents an individual measurement unit, pooled from n = 3 mice (biological replicates) per group (Old, Young); no technical replicates were pooled within a mouse. Precise cell numbers per group are reported in Supplementary Table 3 the embedded box plots show the median as the center line, the 25th and 75th percentiles as the lower and upper bounds of the box, and whiskers extending to the most extreme values within 1.5× the interquartile range above and below the box; values beyond the whiskers are plotted as outliers. The outer violin shape represents the kernel density estimate and does not indicate the observed minimum or maximum. P values were calculated using a two-sided Mann-Whitney U-test.

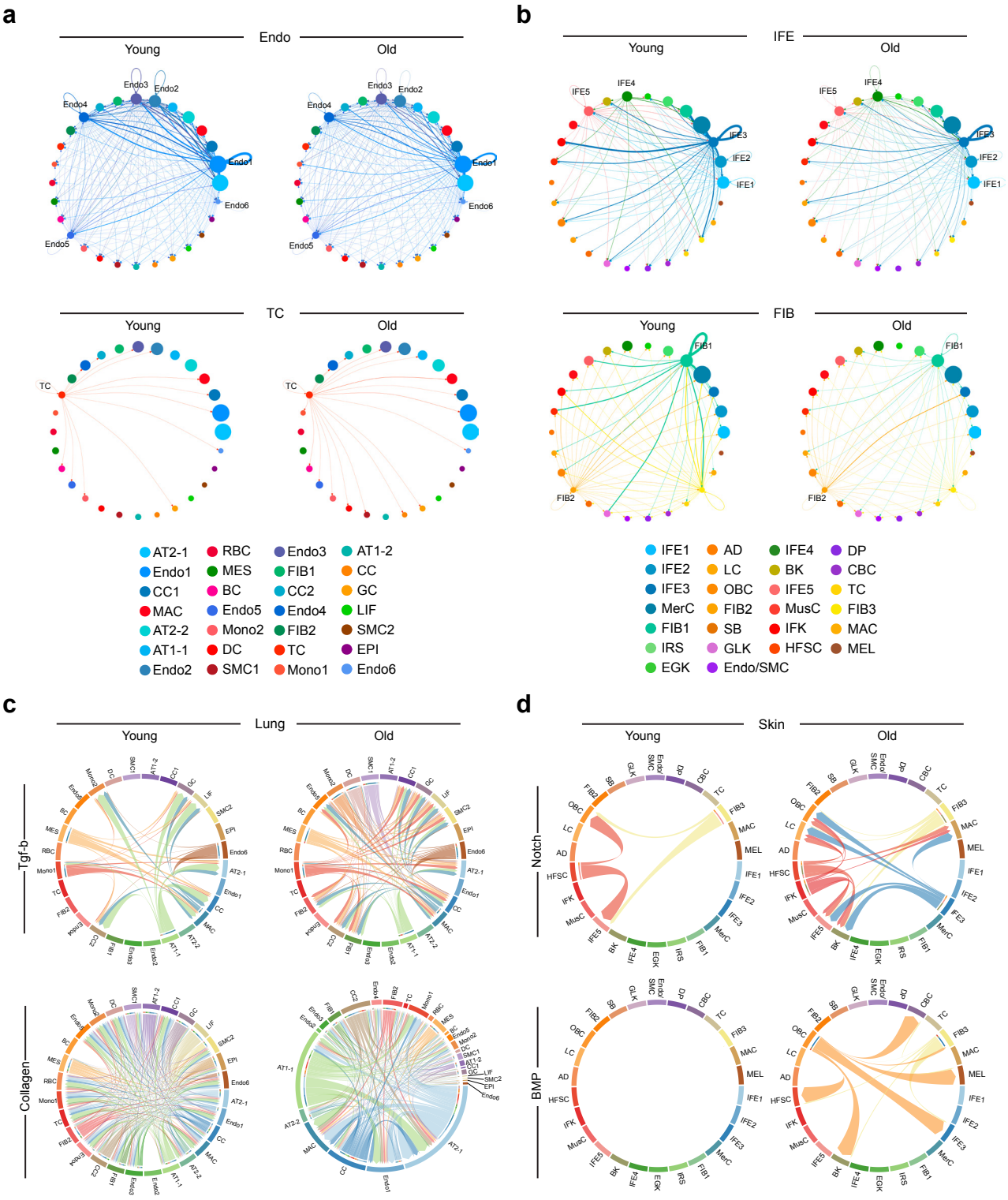

Supplementary Fig. 4. Cell type-resolved remodeling of intercellular communication with age in mouse lung and skin.

a, Circle plots showing inferred cell-cell interactions between endothelial cell subtypes (top) or T cells (bottom) with other cell types in old and young mouse lung. Line width reflects the number of inferred ligand-receptor interactions between cell types; thicker lines indicate a greater number of interactions. **b**, Circle plots showing inferred cell-cell interactions between interfollicular epidermis cell subtypes (top) and fibroblast cells (bottom) with other cell types. Line width reflects the number of inferred ligand-receptor interactions between cell types; thicker lines indicate a greater number of interactions. **c-d**, Chord plots showing the communication probability between cell types through specific signaling pathways in mouse lung (**c**) and skin (**d**) in old and young samples. Arrow stem (signaling sender), arrowhead (signaling receiver), arrow width (signaling strength).

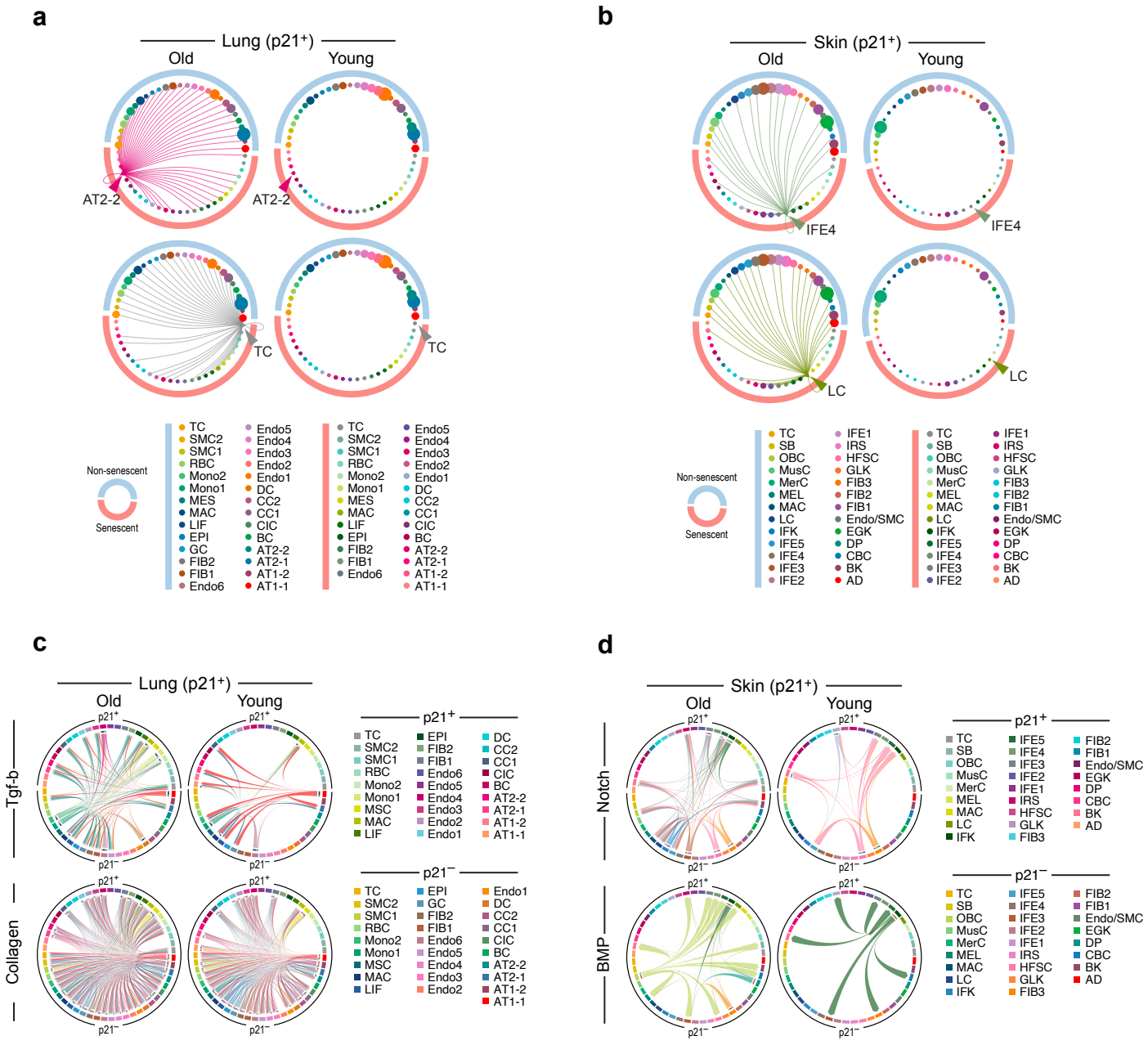

Supplementary Fig. 5. Cell type-resolved remodeling of intercellular communication between senescent and non-senescent cells in mouse lung and skin.

a-b, Circle plots showing inferred cell-cell interactions of *p21*$^{+}$ senescent AT2 and *p21*$^{+}$ senescent T cells with other cell types in old and young mouse lung (**a**), and *p21*$^{+}$ senescent IFE4 cells and senescent *p21*$^{+}$ LC with other cell types in mouse skin (**b**) at different ages. Line width indicates the interaction strength. **c-d**, Chord plots showing the communication strength between *p21*$^{+}$ senescent and *p21*$^{-}$ non-senescent cell types through specific signaling pathways in mouse lung (**c**) and skin (**d**) in old and young samples. Arrow stem (signaling sender), arrowhead (signaling receiver), arrow width (signaling strength).

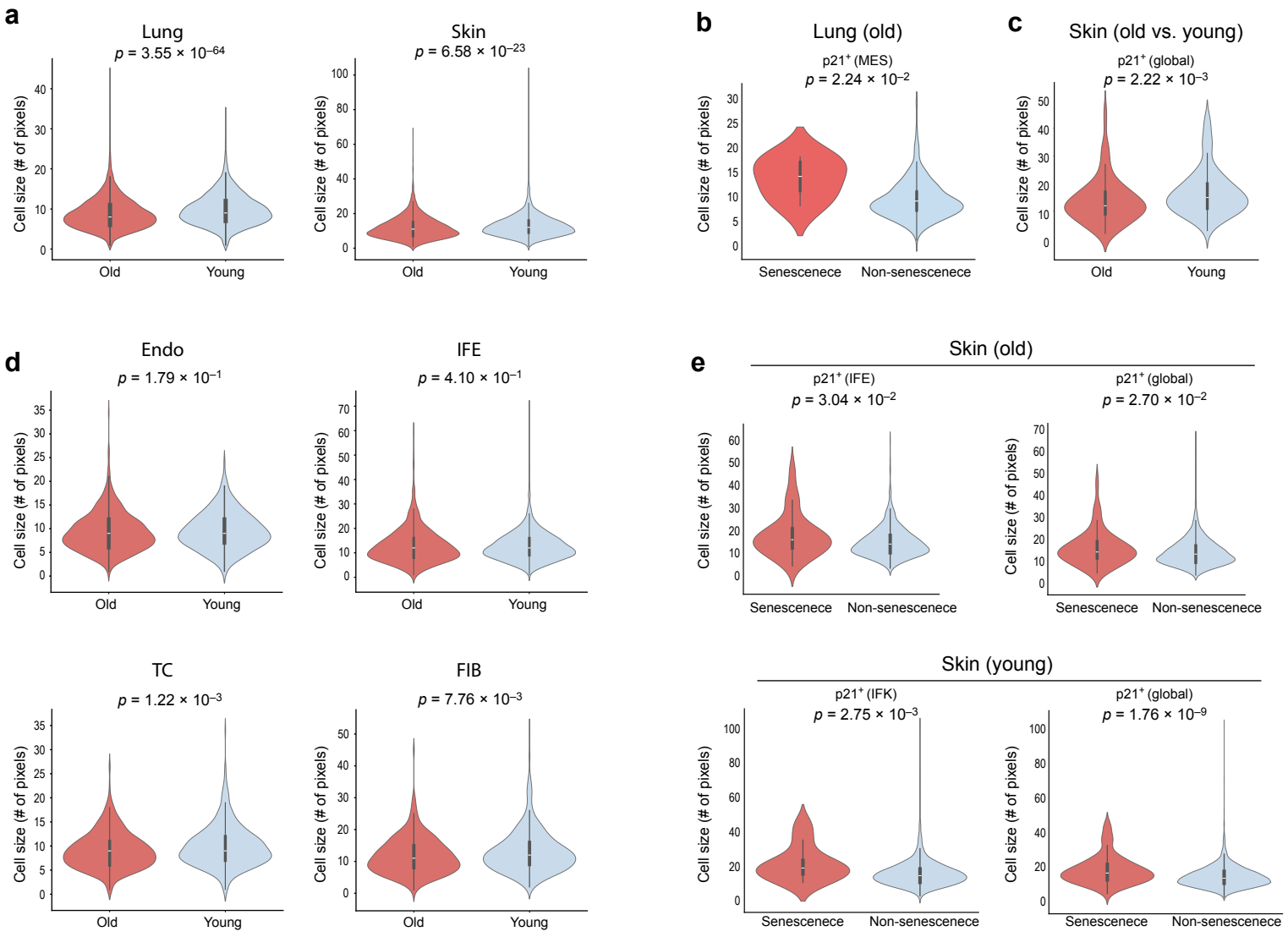

Supplementary Fig. 6. Comparative analysis of cell size differences across tissues, ages and senescence status.

a, Violin plots showing the distribution of cell size quantified by the number of Raman pixels per cell in old and young mouse lung and skin at tissue level. **b**, Violin plot showing cell size measured by the number of Raman pixels per cell in *p21*$^{+}$ and *p21*$^{-}$ cells from old mouse lung mesenchymal cells. **c**, Violin plots showing cell size measured by the number of Raman pixels per cell in *p21*$^{+}$ senescent cells from young and old mouse skin at tissues. **d**, Violin plots showing cell size quantified by the number of Raman pixels per cell across cell types in young and old mouse lung and skin. e, Violin plots showing cell size measured by the number of Raman pixels per cell in *p21*$^{+}$ senescent cells and *p21*$^{-}$ non-senescent cells from young and old mouse skin, shown at tissue level and within IFE and IFK cell populations as indicated. For **a-e**, each cell represents an individual measurement unit, pooled from n = 3 mice (biological replicates) per group (Old, Young); no technical replicates were pooled within a mouse. Precise cell numbers per group are reported in Supplementary Table 3 the embedded box plots show the median as the center line, the 25th and 75th percentiles as the lower and upper bounds of the box, and whiskers extending to the most extreme values within 1.5× the interquartile range above and below the box; values beyond the whiskers are plotted as outliers. The outer violin shape represents the kernel density estimate and does not indicate the observed minimum or maximum. P values were calculated using a two-sided Mann-Whitney U-test.